Pulsed RF heating simulations in normal-conducting L-band cavities.

V.V. Paramonov, A.K. Skasyrskaya
Institute for Nuclear Research, 117312, Moscow, Russia

Abstract

In some special parts of present projects, such as X-FEL and ILC, normal conducting cavities are applied, operating with high electric and magnetic fields. RF gun cavities with an electric field up to $60\frac{MV}{m}$ at the photo cathode are now under development. Capture cavities in the ILC positron source should operate with an accelerating gradient of up to $15\frac{MV}{m}$, practically the same value ($14\frac{MV}{m}$), as for the CDS booster cavity in the Photo Injector Test Facility at DESY in Zeuthen (PITZ). Such operating conditions, together with long ($\sim 1ms$) RF pulse, lead to the apparent cavity pulsed heating effect.
In this report we describe the procedure and results of pulsed heating effect simulations in L-band cavities, operating with high pulsed RF loss density and long RF pulse.

1 Introduction

The source for cavity heating is RF losses, generated during RF pulse, due to final cavity material conductivity, in the thin surface skin layer. The thickness of this surface layer, the skin depth δ:

$$\delta = \sqrt{\frac{1}{\mu_0 \pi f \sigma_c}}, \quad R_s = \sqrt{\frac{\mu_0 \pi f}{\sigma_c}}, \tag{1}$$

is $\sim 2\mu m$ for operating frequency $f = 1300MHz$. In (1) σ_c is the copper electric conductivity, R_s is the copper RF surface resistance, $R_s = 9.4 \cdot 10^{-3} Ohm$.
With a pulsed cavity operation, cavity heating is also a pulsatile process. Once generated in thin surface layer, heat starts propagating from the surface into the cavity body. But it is a slow process, with a typical velocity $\sim \frac{cm}{sec}$. The own copper heat conductivity is not sufficient to transfer all the heat, generated in a surface layer, into the cavity body for the time of a RF pulse. Surface temperature rise takes place. Between RF pulses, heat leaves the heated surface layer, surface temperature decreases and temperature distribution in the cavity body comes to 'average' (over time) distribution. But, another RF pulse arrives and cycle repeats.
For the pulsed heating the pulse dissipated RF power (equal to the input RF pulse power P_i) and a related pulse surface density power P_d are of main importance, $P_d = \frac{R_s H_\tau^2}{2}$, where H_τ is the magnetic field strength at the cavity surface. Average dissipated RF power P_a defines the average temperature distribution in the cavity body. For $10Hz$ repetition rate operation with a RF pulse duration of $1ms$ we have $P_a = 0.01 P_i$.
RF pulsed heating is a well known problem for a very high frequency ($\geq 3 \cdot 10^9 Hz$), high RF power hardware and makes conditional upon wishes for high electric fields. There are a lot of papers describing this topic study, for example [3] and related references. At L-band frequency the maximal electric and related magnetic fields are lower. Together with a lower surface resistance $R_s \sim \sqrt{f}$, it leads to lower (in order) values of maximal dissipated RF power density P_d, as compared, for example, with X-band NLC or $30GHz$ CLIC accelerating

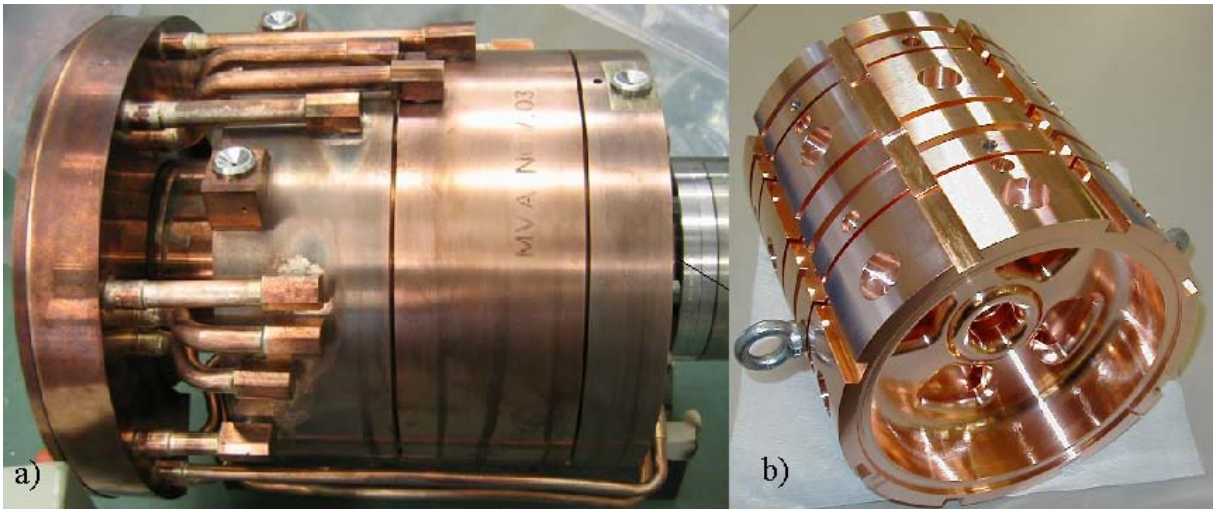

Figure 1: DESY L-band 1.5 cell RF Gun cavity (a) and CDS booster cavity cells (b).

structures. For some special L-band cavities, operating with significant field values, the pulsed surface RF heating also takes place.

For example, during DESY L-band 1.5 cell RF Gun cavity, (Fig. 1a, [1]) operation with the RF electric field at the cathode $E_c = 60\frac{MV}{m}$, the maximal magnetic field at the surface H_{smax} will be $\sim 100\frac{kA}{m}$, resulting in the maximal pulse RF losses density $P_{dmax} = 4.7 \cdot 10^7 \frac{W}{m^2}$. For CDS booster cavity cells (Fig. 1b, [2]) $H_{smax} \sim 55\frac{kA}{m}$ at the end of coupling windows for operating accelerating gradient $E_0T = 14\frac{MV}{m}$, resulting in power pulse loss density $P_{dmax} = 1.42 \cdot 10^7 \frac{W}{m^2}$. These are rather significant (for pulsed heating effect) values. But this effect becomes apparent in L-band NC cavities mainly due to long ($\sim 1ms$) RF pulse.

2 Heat propagation.

We can understand some main properties of the heat propagation using a simple model. Let us consider the pulsed heating of the cylindrical segment (Fig. 3a), uniformly (over the surface) heated at the internal surface with a power loss density $P_d = 4.37 \cdot 10^7 \frac{W}{m^2}$. For such a model we can solve the heat propagation problem by different methods and compare the results.

We assume a classical model of the heat propagation in the homogeneous isotropic body, described by equation:

$$\mathbf{div\ grad}T(\vec{r},t) + \frac{1}{k}g(\vec{r},t) = \frac{1}{\alpha_d}\frac{\partial T(\vec{r},t)}{\partial t}, \quad \alpha_d = \frac{k}{\rho c_\epsilon}, \tag{2}$$

with the initial temperature distribution $T(\vec{r},0) = F(\vec{r})$. If it is not mentioned specially, we will assume $F(\vec{r}) = 0$. In equation (2) the term $g(\vec{r},t)$ represents the volumetric heat source. We can consider the problem in two ways. In the first one we consider a more realistic case, when the heat source is RF losses, distributed in a very thin layer with a skin depth $\delta \sim 2\mu m$ with exponential decay $exp(-r/(2\delta))$ along the distance r into segment body and zero heat flux boundary condition at the inner surface. In the second way we consider the heat source as a prescribed heat flux at the inner surface $r = r_{in}$. One can check directly (but with huge

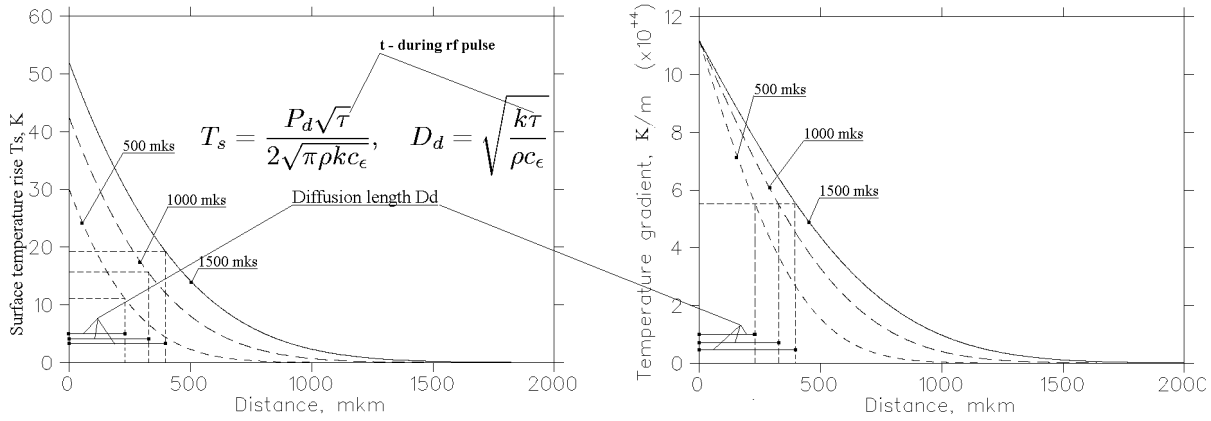

Figure 2: Temperature (a) and temperature gradient (b) distributions near surface for pulse heated OFE tube for different RF pulse length, $P_d = 4.37 \cdot 10^7 \frac{W}{m^2}$.

calculations) - the difference in temperature distribution $T(r)$ in the body is negligible, and takes place only in the skin layer. The first approach is more complicated for simulations even for 1D approximation and can not be realized for 3D Finite Elements Method (FEM) simulations with ANSYS. So, in future we consider $g(\vec{r}, t) = 0$ and use the prescribed heat flux boundary condition at the inner surface:

$$k(\vec{n}\mathbf{grad}T) = P_s, \qquad P_s = 0, t < 0, \qquad , P_s = P_d, 0 < t < \tau, \qquad P_s = 0, \tau < t. \tag{3}$$

In equations (2), (3) $\rho = 8.95 \cdot 10^3 \frac{kg}{m^3}$, $k = 391 \frac{W}{m \cdot K}$ and $c_\epsilon = 385 \frac{J}{kg \cdot K}$ are the density, the heat conductivity and the specific heat for OFE copper, respectively. The copper thermal diffusivity is $\alpha_d = 1.135 \cdot 10^{-4} \frac{m^2}{sec}$.
For our model of the cylindrical segment the problem is one dimensional and heat propagation takes place only in radial direction. Anyhow, even for 1D approximation we cannot solve the problem in a simple analytical form. A solution, based on Green's function technique, is given in [3] and also requires numerical calculations for special functions. To have the reference temperature distributions, we apply direct numerical integration for equation with boundary conditions (3).
Numerically integrated (1D) temperature $T(r)$ and gradient $G(r)$ distributions are shown in Fig. 2.

Two parameters are most important for this effect description - a surface temperature rise T_s at the RF pulse τ time with respect the initial temperature value before RF pulse, and a diffusion length D_d - the distance of temperature decreasing (along the normal direction inside cavity body) e times, see for example, [4]:

$$T_s = \frac{P_d\sqrt{\tau}}{2\sqrt{\pi\rho k c_\epsilon}}, \quad D_d = \sqrt{\frac{k\tau}{\rho c_\epsilon}} = \sqrt{\alpha_d \tau}, \quad T_s = \frac{P_d D_d}{2\sqrt{\pi} k}, \tag{4}$$

These analytical expressions were obtained in 1D approximation. During RF pulsed heating we have heat propagation from the surface into cavity body with rather sharp temperature front. For the pulse length $\tau = 0.5ms; \quad 1.0ms; \quad 1.5ms$ the D_d values (4) are $D_d = 238\mu m; \quad 337\mu m; \quad 413\mu m$ respectively. Due to low propagation velocity at the time of $\sim (1 \div 2)ms$ heat penetrates into the cavity body at the length of $\sim 2D_d$ and the heated

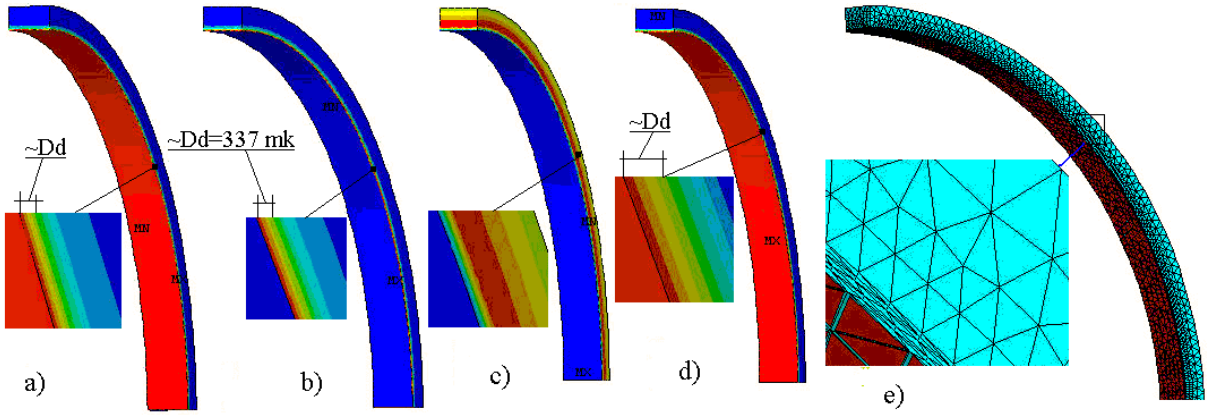

Figure 3: FEM simulated temperature (a), temperature gradient (b), displacements (c) and stress (d) distributions for pulse heated segment of OFC tube, $P_d = 4.37 \cdot 10^7 \frac{W}{m^2}$, $\tau = 1ms$, (e) - the mesh example for 'shell' analysis.

layer can be considered as a thin shell at the cavity surface. In normal n (to the cavity surface) direction we have fast change both in temperature $T(n)$ and in temperature gradient $G(n)$, Fig. 1.3.
The surface temperature rise finishes together with a RF pulse finish. Between RF pulses a temperature distribution smoothing takes place - the heat propagates from the heated surface layer into the cavity body. Surface temperature decreases fast- for $t = 2\tau$, $T = 0.41T_{smax}$, for $t = 10\tau$, $T = 0.18T_{smax}$. Temperature distribution at the cavity surface aspires to 'average' over time value.

2.1 Numerical Procedure

To investigate 3D cavities, we improve our previous procedure of the closed-loop 3D cavities analysis [5]. A special meshing technique has been developed (Fig. 1.4e) to ensure precise complete thermal-stress analysis in very thin ($\sim (1.5 \div 2.0)D_d$) 3D shell layer at the surface of relatively big $\approx 200mm$ cavity, together with the cavity itself, with reasonable computing resources. The thermal analysis is performed by direct numerical solution of non-stationary heat transfer equation (2) for the time of RF pulse τ using usual ANSYS possibilities.
The procedure has been tested at the segment of uniformly pulsed heated tube, considered above, where thermal parameters and distributions were precisely calculated with another way, Fig. 2.

In our simulations we integrate equation (2) with a time step $dt \sim 5\mu s$ during RF pulse. Numerically calculated T_s value at the cavity surface is not so sensitive to the mesh size and time integration step, if $dt < 10\mu s$, and well coincides with the value, obtained with estimation (4). Relative difference is $\sim 10^{-4}$.
To obtain correct temperature distribution in normal direction, which is important for reliable stress problem solution, we need a dense mesh, even using second order elements. But small element size is only required in normal direction. To provide controlled mesh, with small mesh size in normal and relatively large one in tangential directions, we generate a special solid model, Fig. 4, with a special multi-layers shell at the cavity surface, which is a part of the cavity body. The layers number in the shell and each layer thickness depend

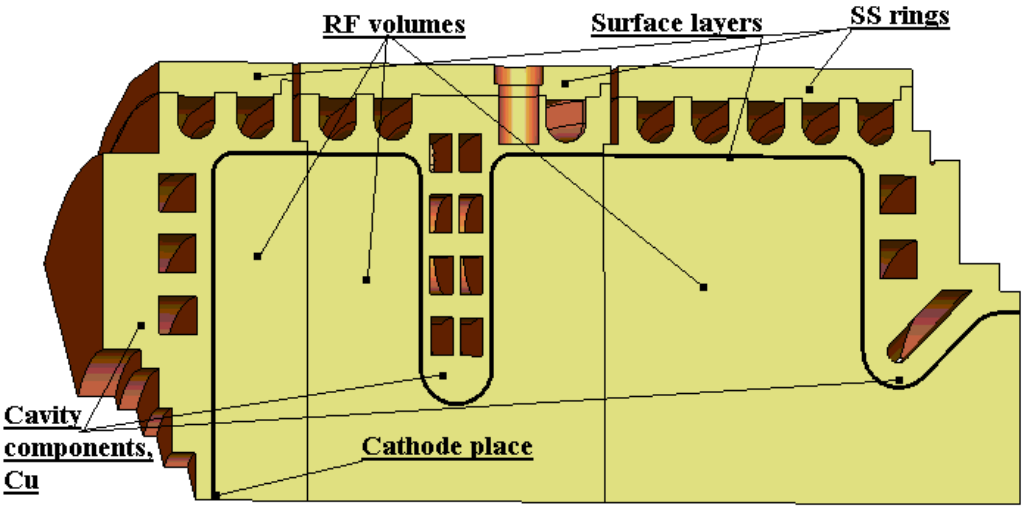

Figure 4: Solid model for RF Gun cavity pulsed heating simulations.

on the heat propagation distance during the RF pulse. The total shell thickness should be $(\sim (1.5 \div 2.0)D_d)$ with mesh size in normal direction $(\sim (0.2 \div 0.3)D_d)$ - it is necessary for numerical approximation of both temperature (Fig. 1.3a) and temperature gradient (Fig. 1.3b) distributions at the length of fast changing.
Numerical simulations with finite elements are a consuming procedure with respect to computer memory and CPU time requirements and we are limited with total mesh-points number. To keep reasonable compromise between description of thin layers and remaining cavity body, together with RF volume, we can place in layers approximately half of the total number of mesh points. With the reasonable mesh-size $(\sim 100\mu m)$ in layers along the normal direction, we have to restrict our model with minimal part of the total geometry - 1/8 for RF Gun cavities with rotational symmetry and 1/4 for CDS one. We also restrict the numerically considered RF pulse length with $1ms$. For longer RF pulses scaling relations and given above time dependencies should be used. In our FEM simulations we assume constant values for material parameters. For the practical P_d and τ values the surface temperature rise T_s is significant to provide apparent effect on cavity parameters, but is not significant for sufficient change in material properties. The simulations with temperature dependent material parameters are much more consuming in CPU time, but the difference of final results for considered practical cases - frequency shift values, is in the range of precision for such simulations.

3 Calculated surface temperature rise due to RF pulsed heating for RF Gun cavities

DESY RF Gun cavities have two (or 1.5 in some references) cells. At the cathode, Fig. 4, is the electric field E_c and E_2 is maximal E_z value at the cavity axis in the second cell. For tuned RF Gun cavity should be $F_{rat} = \frac{E_c}{E_2} = 1$. According to RF Gun philosophy, the maximal electric axis field should be at the cathode. In the second cell the maximal electric field at cavity axis can be in limits $E_2 \sim (1.0 \div 0.9)E_c, 1.1 \geq F_{rat} \geq 1.0$ [6].

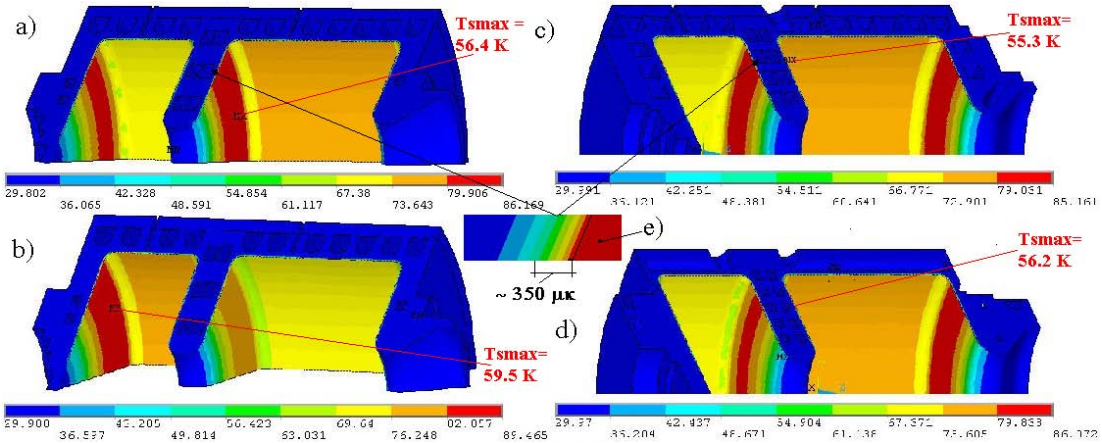

Figure 5: Temperature rise T_s distributions at the surface of RF Gun cavities. $\tau = 1000\mu s$, $P_i = 8MW$. a) - Gun 3, $F_{rat} = 0.979$, b) - Gun 3, $F_{rat} = 1.10$, c) - Gun 4, $F_{rat} = 1.00$, d) - BESSY Gun, $F_{rat} = 0.944$, e) - a surface temperature distribution in normal direction into cavity body, enlarged scale.

The BESSY Gun [7], also considered for the pulsed heating effect, has the same RF volume shape, as DESY Guns, but has quite different design of cooling circuit and is totally constructed from copper components. In this case, for temperature simulations, and especially for further cavity deformation simulations we have no problem with correct definition of thermal and elastic parameters of cavity components.

The temperature rise T_s distributions are shown in Fig. 5 for Gun 3, Gun 4 and BESSY Gun cavities, assuming that input RF power is $P_i = 8MW$ and RF pulse length is $\tau = 1000\mu s$. During RF pulse, heat penetrates into the cavity body at a length of $\sim 2D_d \leq 1mm$. For $\tau = 1000\mu s, = 2000\mu s$, and $\tau = 3000\mu s, D_d = 337\mu m, = 413\mu m$ and $D_d = 447\mu m$, respectively. All elements of the cavity design, such as cooling channels, as a rule, are placed at larger distance from the surface. Heat propagation in tangential directions during RF pulse is also negligible, due to smooth P_d distribution and small variation in P_d at a distance of $\sim D_d$. Such cavity shape elements, as rounding, also have a curvature radius $> D_d$. For RF pulse length, until D_d is small, there is no heat reflection from internal cavity design elements and there is no essential deviation from 1D model of heat penetration into the cavity body, the cavity engineering design is not important for pulsed thermal effect. At the cavity surface T_s (1) distribution repeats very well the P_d one. **For the given cavity and operational regime there are no methods for the pulsed surface temperature rise control.**

One can see confirmation of this statement in temperature distributions, shown in Fig. 5. All RF cavities, shown in Fig. 5, have the same RF field distribution inside the cell. The final P_d distribution depends on the field balance between the cells. We also have to remember that $P_d \sim E^2_{c,2}$. Perfectly tuned case $F_{rat} = 1.0$ leads to the temperature distribution, shown in Fig. 5c for Gun 4 cavity. As one can see from Fig. 5c, the surface temperature rise in the second sell is higher than in the cathode half cell. The temperature distribution, shown in Fig. 5b corresponds to tolerable fields ratio $F_{rat} = 1.1$. Comparing temperature distributions in Fig. 5a, Fig. 5b, and taking into account the corresponding F_{rat} values, one can understand the difference - in the example, shown in Fig. 5a the maximal surface

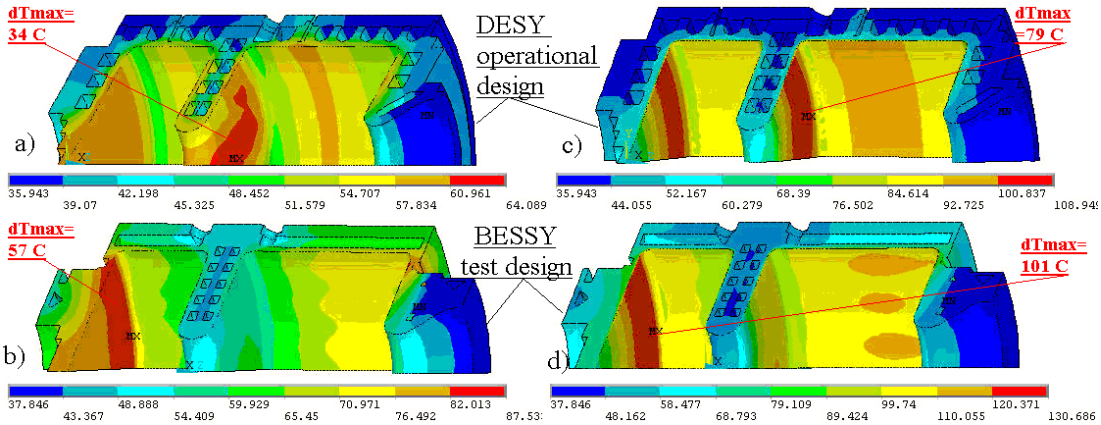

Figure 6: Surface temperature distributions just before (a,b) and just after (c,d) RF pulse for DESY Gun4 (a,c) and BESSY Gun (b,d) cavities. $E_c = 60\frac{MV}{m}, \tau = 1000\mu s, RR - 10Hz$.

temperature is in the second cell, and for example, shown in Fig. 5b - in the first one. Also comparing temperature distributions, shown in Fig 5, one can see that reasonably significant spread in F_{rat} value, from 0.944 to 1.1, doesn't result in proportional spread of the maximal surface temperature.
In the thin heated layer a rather big heat energy W_h is deposited during RF pulse, $W_h = P_i\tau \sim (6 \div 7)kJ$ for $E_c = 60\frac{MV}{m}$ operation.

3.1 Total surface heating for RF Gun cavities

We should remember that the pulsed RF surface heating is an additional temperature effect, which, for the cavity surface, arises during RF pulse and is added to the stationary average surface temperature due to the average cavity heating, related with a high value of average dissipated RF power. The pulsed surface temperature rise is sharp splashes, added to the average surface temperature T_{s-av}. Let us define T_{s-av} as the steady-state temperature supposing continuous cavity heating with average RF power P_a. It is a good approximation for surface temperature distribution before RF pulse. In Fig. 6 the temperature distributions are shown for Gun 4 and BESSY Gun just before and just after RF pulse.
The average RF power assumed for T_{s-av} simulation is $P_A \approx 67kW$, cooling water temperature is $30C^o$. For average heating the maximal temperature value takes place also at the cavity surface. The cavity engineering design and cooling regime are important for T_{s-av} value and, hence, for maximal surface temperature values after RF pulse.
It should be pointed out here that precise simulation of average temperature distribution is a separate problem and distributions in Fig. 6 have the main purpose to show that we have a sufficiently high surface temperature even for average heating, and to this value a significant addition will be applied due to pulsed temperature rise, resulting in unexpectedly high surface temperature value during the main part of RF pulse.

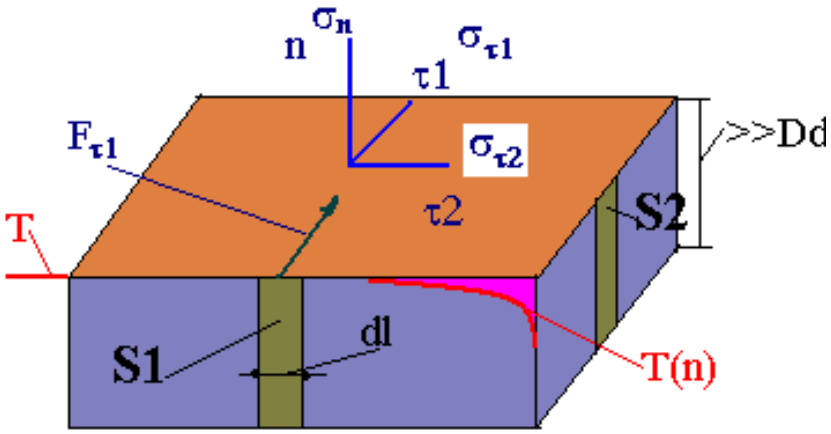

Figure 7: The schematic sketch of a thin non uniformly ($T(n)$) heated film at the surface of a body.

4 Cavities pulsed deformations due to pulsed RF heating

Due to RF pulsed heating, at the surface of the cavity there exists a non uniformly heated thin layer which expands, both in normal $\vec{n}$, and tangential $\vec{\tau}_1, \vec{\tau}_1$, directions. In Fig. 7 a schematic sketch is shown for thin non uniformly ($T(n)$) heated film at the surface of a body. The general equation of thermal expansion is [8]:

$$\frac{3(1-\nu)}{1+\nu}\mathbf{grad\ div}\vec{\mathbf{x}} - \frac{3(1-2\nu)}{2(1+\nu)}\mathbf{rot\ rot}\vec{\mathbf{x}} = \alpha\mathbf{gradT}, \tag{5}$$

where $\alpha = 1.67 \cdot 10^{-5}\frac{1}{K}$, $\nu = 0.345$ and $E_{el} = 1.23GPa$ are the linear expansion coefficient, Poisson ratio and Young module for fully annealed OFE copper. Considering 1D approximation, from (5) one can find:

$$\frac{3(1-\nu)}{1+\nu}\frac{\partial^2 x_n}{\partial^2 n} = \alpha\frac{\partial T}{\partial n}, \quad \frac{3(1-\nu)}{1+\nu}\frac{\partial x_n}{\partial n} = \alpha T, \quad u_{nn} = \frac{\partial x_n}{\partial n} \tag{6}$$

From general relation between principal displacements and stresses [8] we have:

$$\sigma_n = \frac{\alpha T E_{el}}{3(1-2\nu)}, \quad \sigma_{\tau_{1,2}} = \frac{\alpha T E_{el}\nu}{3(1-2\nu)(1-\nu)}, \tag{7}$$

For normal displacements x_n, from (6) it directly follows that $x_n \sim \int T(n)dn$. The stresses $\sigma_n, \sigma_{\tau_{1,2}}$ have the dimension of the pressure, which is the force, applied to the unit surface. To evaluate the force values in tangential directions, we have to integrate $\sigma_{\tau_{1,2}}$ over surface S_1 and S_2, see Fig. 7, respectively:

$$F_{\tau_{1,2}} = \int_{dS_{1,2}} \sigma_{\tau_{1,2}} dS = dl \int \sigma_{\tau_{1,2}} dn \sim dl \int T(n)dn. \tag{8}$$

For elastic deformations $x_i \sim F_i$, but proportionality coefficient between x_i and F_i depends on the cavity design, material and constrains under mounting. Taking it into account and

multiplying $\int T(n)dn$ by c_ϵ value, we get:

$$x_i \sim F_i \sim \frac{\int c_\epsilon T(n)dn}{c_\epsilon} \sim \frac{W_h}{c_\epsilon} \tag{9}$$

for all components of the displacements. According to the perturbation theorem, the cavity frequency shift δf for small surface displacements is:

$$\delta f \sim x_i \sim F_i \sim \frac{W_h}{c_\epsilon}. \tag{10}$$

Basing on the above given relations, we can formulate the following conclusions for deformations of pulsed heated cavities:
a) - the stress values in the thin heated layer are proportional to the layer temperature rise, until we neglect material properties change with this rise and the heated layer is thin;
b) - the deforming forces and induced displacements are proportional to the heat value, deposited in the layer, but depend on the cavity design, material and constrains under cavity mounting;
c) - for the constant RF input power, the heat value, deposited in the layer, is proportional to the time during RF pulse;
d) - the cavity frequency shift is proportional to the time from the RF pulse beginning;
and the parameter

$$S_f = \frac{\delta f}{\tau P_i}, [\frac{kHz}{ms \cdot MW}], \tag{11}$$

is the property of the given cavity and can be used to estimate the cavity frequency shift for different RF input power levels and RF pulse length.
The estimations (5), (10) describe general relations. For complicated cavity geometry, taking into account cavity engineering design, the parameter S_f should be defined in numerical simulations. Especially for these simulations (numerical solution of equation (5)) the mesh parameters in multi layer film at the cavity surface, see Fig. 3e, Fig. 4, are extremely important. Comparing results of our numerical simulations for the model, shown in Fig. 3, with analytical solution (one can find it in [8]), for our solid model, shown in Fig. 4 , (with appropriate mesh parameters), we can estimate the relative errors in S_f and σ_i calculations at the level $\pm(15 \div 20)\%$.

5 Calculated pulsed deformations and frequency shifts for RF Gun cavities.

In Fig. 8 the distributions of displacements, induced by pulsed heating, for DESY Gun 3 (Fig. 8a,a1,a2), Gun 4 (Fig. 8b,b1,b2) and BESSY Gun (Fig. 8c,c1,c2) after the end of RF pulse with $\tau = 1000\mu s$, $P_i = 8MW$ are shown. In Fig. 8a,b,c one can see the total displacements, in Fig. 8a1,b1,c1 the radial components of displacements, and in Fig8 a2,b2,c2 - the longitudinal ones. In simulations the left side of the cavity is rigidly fixed, the right one is free. In each picture the maximal value of appropriate displacement is printed in micrometers.

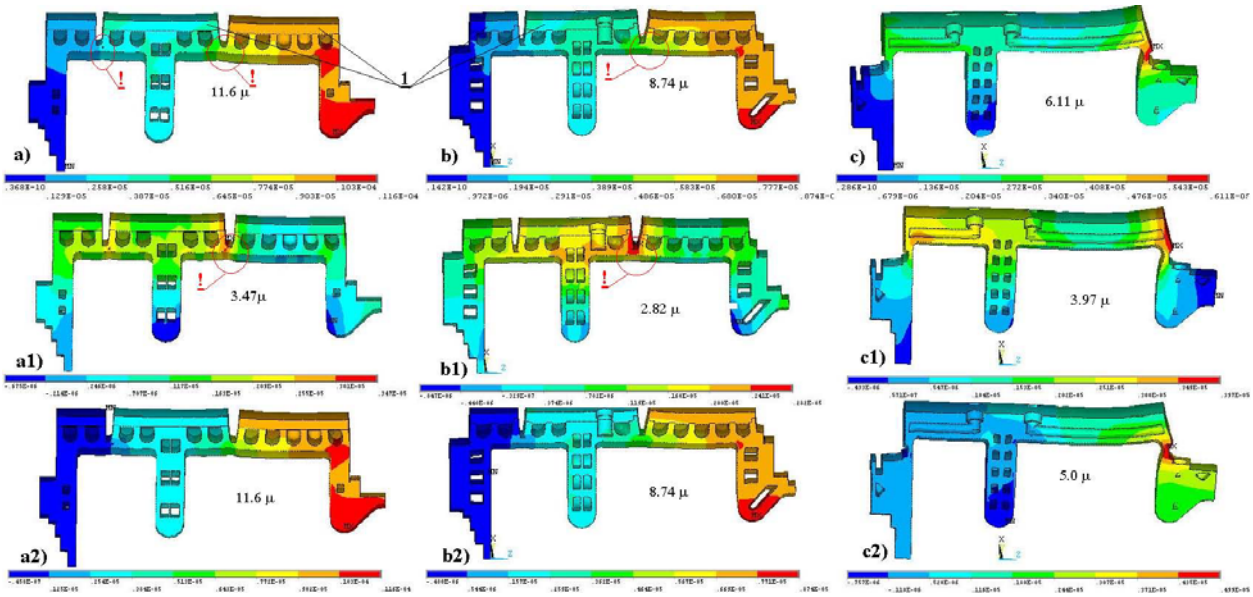

Figure 8: Displacements, induced by pulsed heating, for DESY Gun 3 (a,a1,a2), Gun 4 (b,b1,b2) and BESSY Gun (c,c1,c2) cavities after the RF pulse end with $\tau = 1000\mu s$, $P_i = 8MW$. a), b), c) - the total displacements; a1), b1), c1) - the displacements in radial direction; a2), b2), c2) - the displacements in longitudinal direction. The left side of the cavity is rigidly fixed, the right one is free. 1 - segregated stainless steel jacket in DESY Guns design.

All DESY Gun cavities have a Stainless Steel (SS) jacket, Fig. 8, which improves the cavity rigidity. The BESSY Gun cavity is constructed totally from OFE copper. In this case we remove one degree of possible uncertainty in simulations - for a cavity with uniform material the calculated values of displacements and the corresponding frequency shift do not depend on material Young module value.

As one can see from Fig. 8a,b,c, the total displacements picture is rather complicated and depends on cavity design. Especially large qualitative difference in deformations we see, comparing DESY Guns and BESSY Gun designs. Qualitatively, the displacements values are of order $\approx 10\mu$ for all considered cavities under the conditions of RF pulse applied. The stress values, caused by such deformations, ($\approx 10^7 Pa$), lie well below the copper yield limit, and cavity deformations are elastic. The energy W_{el}, stored in elastic deformations, (for the conditions of RF pulse applied) is $W_{el} \sim 2J \ll W_h \sim 7kJ$. It is by a factor 10^3 smaller than the heat energy W_h, stored in the thin heated layer. In this case we can consider the effects of pulse heating and induced deformations as independent ones.

RF Gun cavities are naturally closer to cylindrical shape, and we specially show in the pictures radial x_r components (Fig. 8a1,b1,c1) and longitudinal x_z ones (Fig. 8a2,b2,c2), to emphasize cavity elements displacements in transversal and longitudinal directions.

The calculated S_f values are $S_f \approx -3.0\frac{kHz}{ms \cdot MW}$ for DESY Gun 3, $S_f \approx -2.7\frac{kHz}{ms \cdot MW}$ for DESY Gun 4 and $S_f \approx -3.8\frac{kHz}{ms \cdot MW}$ for BESSY Gun. In general, there are no big differences in the value of frequency sensitivity to the pulsed heating between considered Gun designs. Lower values for DESY Guns can be explained well by SS jacket influence, which restricts the radial displacements in the cavity. The operating mode in Gun cavities cells can be classified as the TM_{010} one and the frequency shift for such a mode is more sensitive to transversal cell

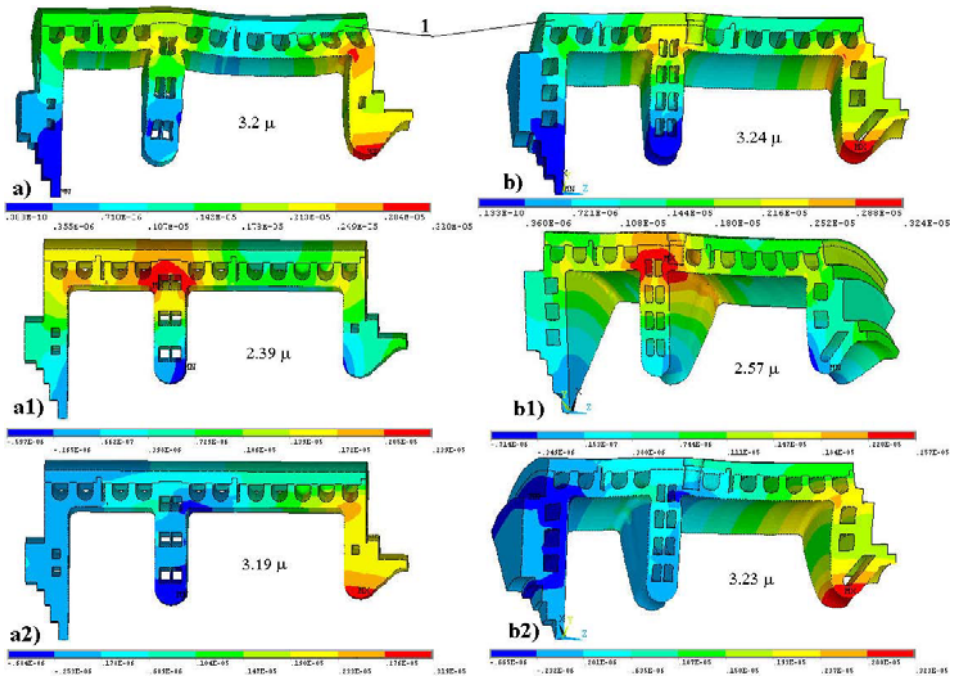

Figure 9: Displacements, induced by pulsed heating, for DESY Gun 3 (a,a1,a2) and Gun 4 (b,b1,b2) cavities after the RF pulse end with $\tau = 1000\mu s$, $P_i = 8MW$. a), b) - the total displacements; a1), b1) - the displacements in radial direction x_r; a2), b2) - the displacements in longitudinal direction x_z. 1 - joint solid stainless steel jacket.

shape displacements.
It should be pointed out here that we **confidently** show the calculated **negative** frequency shift for RF Guns normal design, instead of the **positive** frequency shift value, extracted from the experimental data treatment in [9]. One can see in Fig. 8a1,b1,c1 **negative** radial displacements (inside the cavity) in the cavity regions with a strong electrical field (iris nose) and **positive** radial displacements (outside the cavity) at the outer cylindrical wall (the region with a strong magnetic field). According to perturbation theorem, such displacements should result in frequency decreasing.
The DESY Guns have segregated SS jackets, which conditionally divides the cavity in three parts. Comparing longitudinal deformations for DESY Guns, Fig. 8a2,b2, and for BESSY Gun, Fig. 8c2, one can see approximately uniform (along the cavity length) x_z deformations for BESSY cavity design. For DESY cavities one can pick out three regions in x_z distribution along the cavity. The three cavity parts, each clamped by its own part of the segregated SS jacket, move, approximately, as a unit. The main part of longitudinal deformations, marked by red circles and exclamation marks in Fig. 8, takes place between these cavity parts. Taking into account the pulsed RF operation, these regions of the cavity should get higher cyclic fatigue, as compared to other cavity components. It should be also pointed out that due to cavity design and construction technology in these regions brazed junctions are placed, which are not the strongest element, as compared to solid material.

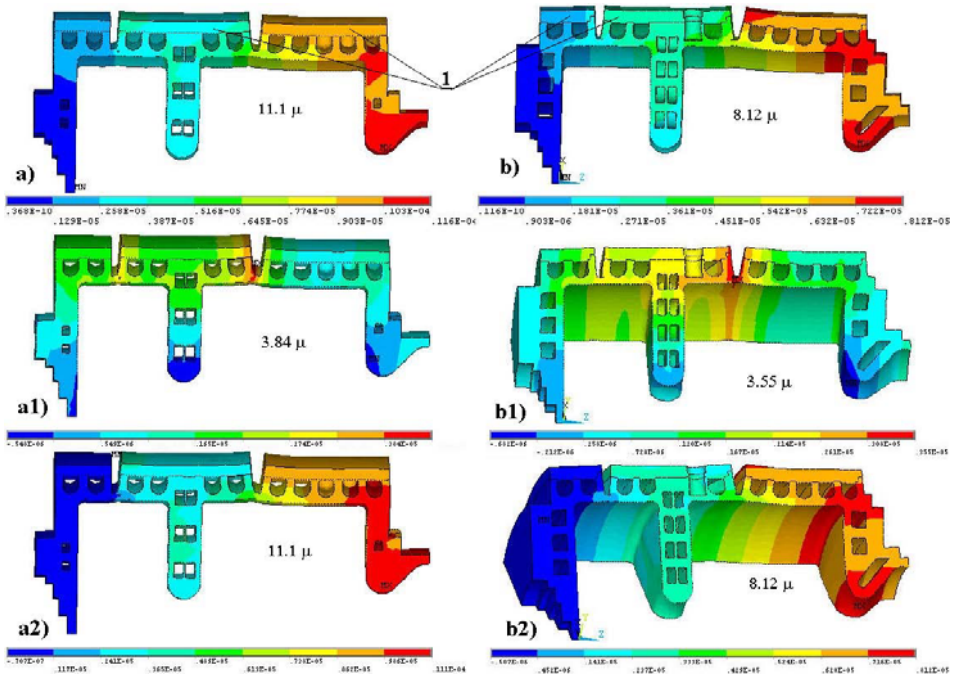

Figure 10: Displacements, induced by pulsed heating, for DESY Gun 3 (a,a1,a2) and Gun 4 (b,b1,b2) cavities after the RF pulse end with $\tau = 1000\mu s$, $P_i = 8MW$. a), b) - the total displacements; a1), b1) - the displacements in radial direction x_r; a2), b2) - the displacements in longitudinal direction x_z. 1 - segregated copper jacket.

5.1 Possible design modifications for RF Gun cavities

In our simulations we can investigate not only normal cavity design, but can also consider some cavity engineering design modifications, to estimate possibilities and limits in the control of the pulsed cavity frequency shift.

In Fig. 9 the distributions of displacements, induced by pulsed heating, for DESY Gun 3 (Fig. 9a,a1,a2) and Gun 4 (Fig. 9b,b1,b2) after the end of RF pulse with $\tau = 1000\mu s$, $P_i = 8MW$, assuming the joint solid SS jackets for the whole cavity, are shown. In Fig. 9a,b one can see the total displacements, in Fig. 9a1,b1 the radial component x_r of displacements, and in Fig.9a2,b2 - the longitudinal x_z component of the displacements.

Comparing the longitudinal displacements values x_z for the normal design with a segregated SS jacket, (Fig. 8a2,b2), and for the joint solid one, (Fig. 9a2,b2), one can see that x_z is reduced several times for the case of joint jacket. Such a jacket restricts the cavity expansion in longitudinal direction. Also longitudinal deformations are more uniform along the cavity - we do not see deformation concentration in the place of brazed junctions. The radial displacements are practically the same in value. But now the maximal x_r value takes place near iris foundation, instead of the places of brazed junctions, as it is for the case of segregated jacket, see Fig. 8a1,b1.

The total cavity shape deformations are smaller for the joint SS jacket case, and are more uniformly distributed in the cavity body. The calculated frequency shift sensitivity values S_f are also lower in the case of joint SS jacket, $S_f \approx -2.32\frac{kHz}{ms \cdot MW}$ for Gun 3 case and $S_f \approx -2.07\frac{kHz}{ms \cdot MW}$ for Gun 4 cavity design.

With respect to the pulsed RF Gun cavity deformations and related frequency shift, the joint

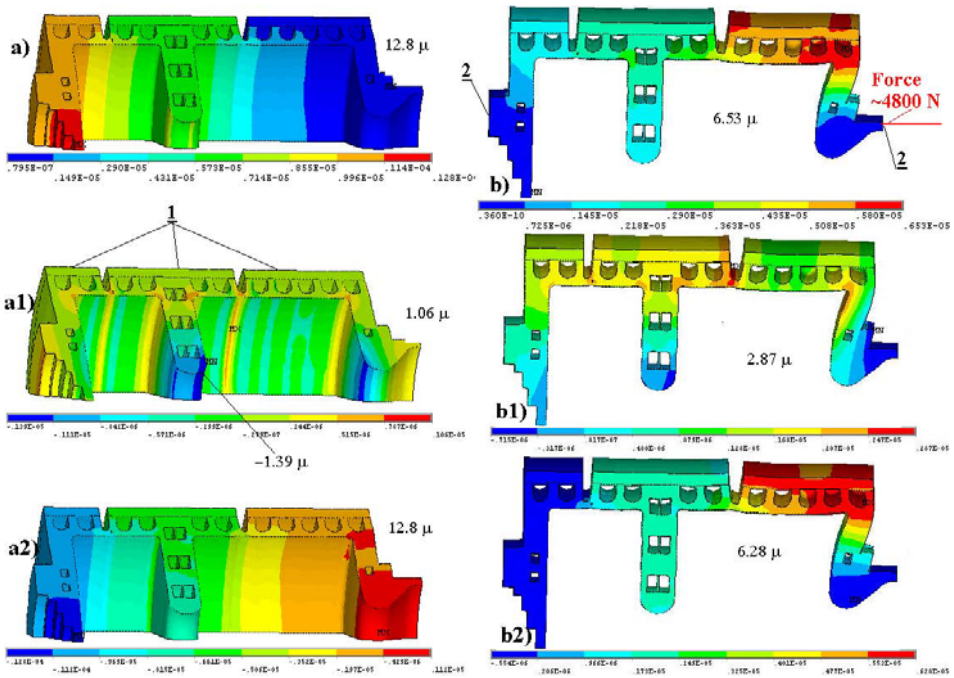

Figure 11: Displacements, induced by pulsed heating, for DESY Gun 3 cavity after the RF pulse end with $\tau = 1000\mu s$, $P_i = 8MW$. a),a1),a2) - the total, radial and longitudinal displacements distributions, respectively, assuming infinitely rigid jacket (1); b),b1),b2) - the total, radial and longitudinal displacements distributions, respectively, assuming rigidly fixed plates (2).

solid SS jacket has a preference of lower cavity deformations, the cavity becomes more rigid, as compared to the design with a segregated SS jacket. But the effect of pulsed deformations remains, just decreases, and technical realization of the joint jacket is more difficult.

Another possible design modification is just opposite, with respect to the joint SS jacket case, considered above. Let us suggest some segregated copper jackets in the Rf Gun design. In Fig. 10 the distributions of displacements, induced by pulsed heating, for DESY Gun 3 (Fig. 10a,a1,a2) and Gun 4 (Fig. 10b,b1,b2) after the end of RF pulse with $\tau = 1000\mu s$, $P_i = 8MW$ are shown, assuming a segregated copper jacket. In Fig. 10a,b one can see the total displacements, in Fig. 10a1,b1 the radial component x_r of displacements, and in Fig.10a2,b2 - the longitudinal x_z component of the displacements.

In this case, as a sequence of the segregated jacket concept, we have practically the same total and longitudinal displacements, as one can see comparing with the values and displacements distributions, given in Fig. 10 and Fig. 8 for the normal case design. There are also displacements concentrations near brazed junctions. The cavity becomes softer and more sensitive to the effect of pulsed deforming forces. The calculated frequency shift sensitivity values S_f are higher, as compared to segregated SS jacket, and $S_f \approx -4.13\frac{kHz}{ms \cdot MW}$ for Gun 3 and $S_f \approx -3.8\frac{kHz}{ms \cdot MW}$ for Gun 4 cavity design.

The option with a segregated copper jacket has no preferences with respect to the pulsed deformations, as compared to the existing design with SS jackets.

5.2 Different constrains for RF Gun cavities

We can also discuss the effect of different cavities constrains, simulating in this way possible restrictions for the mounted cavity and response for the pulsed deformations.
Let us suppose that we prohibit cavity expansion in radial direction by using an infinitely rigid segregated jacket. The distributions of the cavity displacements for this case are shown in Fig. 11a,a1,a2. With the restriction in radial direction, we have slightly enlarged longitudinal displacements, Fig. 11a2. In radial direction we see deformation inside the cavity, Fig. 11a1. In this picture (Fig. 11a1) one can see the evidence of sensitivity for our simulations - blue regions at the cavity inner surface reflect the cooling channels structure inside the cavity wall. The result of frequency shift estimation shows interesting particularity - the calculated S_f value is small enough and has a **positive** sign, $S_f \approx +0.48\frac{kHz}{ms \cdot MW}$.
With the rigid cavity fixation between two plates, we have interesting pictures for cavity deformations, see Fig. 11b,b1,b2. If we keep the RF coupler part rigidly, the outer part of the cavity moves. The calculated S_f value is maximal for all considered Gun 3 cavity options, $S_f \approx -4.65\frac{kHz}{ms \cdot MW}$

6 Pulsed RF heating effect for CDS booster cavity cell

The CDS booster cavity [2] cells, Fig. 12a, have essentially 3D shape with coupling windows and magnetic field concentration at windows ends. For maximal operating regime $E_0T = 14\frac{MV}{m}$ the maximal magnetic field value at the windows is $H_{smax} \approx 56\frac{kA}{m}$.
Calculated distribution of the surface temperature rise T_s after $\tau = 1ms$ RF pulse is shown in Fig. 12b, resulting in $T_{smax} \approx 27C^o$. As one can see, we have in temperature distribution localized hot spots at the windows ends with respect to moderate temperature rise in the main part of the cell surface.

To find correct solution of equation (5) for periodical structure, we have to apply iterative procedure, described in [5], defining equilibrium conditions. The distributions of the total cell deformations and components of deformations in radial, angular and longitudinal directions, are shown in Fig. 12c,d,e,f, respectively. The maximal value of cell deformation is $\sim 1\mu m$, Fig. 12c. It is a rather small value and here can arise a question about precision of such small displacements calculations. But in Fig. 12d one can see the evidence of sensitivity (and related precision) for our model - the hot spots in a radial component of displacements reflect the blind holes positions with a reduced cavity wall thickness. So, our numerical model in deformations simulations reflects very delicate details of the cavity design. To illustrate more evidently the cell deformations, in Fig. 12c,d,e,f the initial, not deformed contour of the cell shape is shown for each component of deformations.
As one can see from the displacements distributions, there are shape deformations inside the cavity at the blind holes positions, Fig. 12d, together with angular expansion of windows ends inside the cavity, Fig. 12e. These deformations are in the region of a high magnetic field and lead to the frequency increasing. Moreover, the interaction of deforming forces, induced by pulsed heating, with the cell (not simple in shape) body results in the longitudinal drift tubes displacement, Fig. 12e. The distance between the drift tubes noses in the accelerating cell increases at $\approx 1\mu m$, also leading to operating frequency increasing. the calculated frequency shift for CDS operating mode is **positive**, $\delta f \approx 4kHz$ after RF pulse $\tau = 1000\mu s$ for operating regime with $E_0T = 14\frac{MV}{m}$. The calculated quality factor decreasing during RF pulse (see below for definition) for CDS booster cavity cells is $\leq 1\%$.

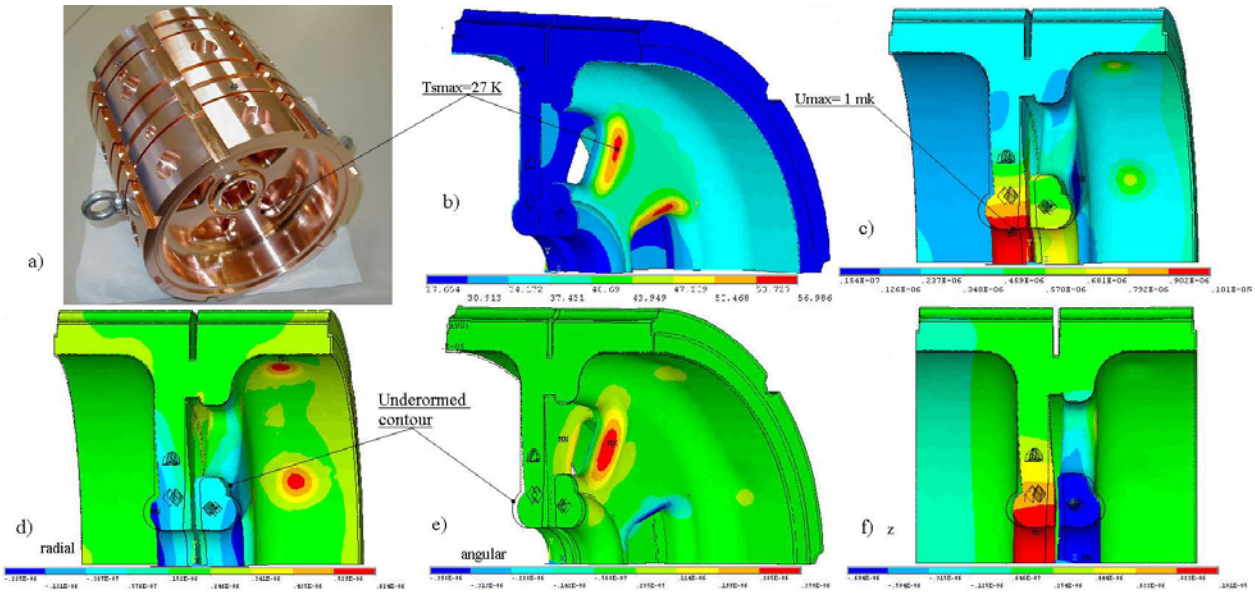

Figure 12: a) - CDS cells, b) temperature rise T_s distributions at the CDS cell surface after $\tau = 1000\mu s$ RF pulse, $E_0T = 14\frac{MV}{m}$, c) the total cell deformations distribution, d),e),f) - the radial, angular and longitudinal components distributions of the cell deformations, respectively.

For periodical structures we cannot introduce the parameter S_f so naturally as it was done for single RF Gun cavities. In this case we provide the frequency shift value and describe conditions. For another operating regime the result scaling is $\delta f \sim \tau \sim (E_0T)^2$.
A CDS structure was considered and proposed for application in normally conducting pre-accelerator [10] in the Positron Source for International Linear Collider (ILC) [11]. The critical point in the PPA structure is the capture sections, which should operate with accelerating gradient $E_0T \approx 15\frac{MV}{m}$ and $\tau = 1000\mu s$ RF pulse length - practically repeating PITZ CDS booster operating regime. For PPA applications a CDS cells shape has been modified slightly for E_{smax} and H_{smax} decreasing. A RF pulsed heating effect in PPA CDS has been considered and compared with such effect in a simple π-mode structure [12], which is another possible option for ILC PS capture sections.
Due to practically the same operating regimes, the pulsed RF heating effect for PITZ CDS and ILC CDS has no big differences. A temperature rise T_s distribution and typical for CDS angular displacements at the windows ends are shown in Fig. 2.7a,c, respectively. In Fig. 2.7b a stress distribution at the cell surface is shown. A maximal stress value, due to pulsed deformations, takes place all the time at the cell surface and for the described operating regime is well below the yield point for OFE copper. The calculated frequency shift after RF pulse is also $\approx +4kHz$, as for PITZ CDS case.
In the simple π-mode structure the magnetic field is more uniformly distributed at the outer cell surface and there are no regions with a strong field concentration, as it is at the CDS windows ends. A temperature rise T_s distribution is shown in Fig. 13d and $T_{smax} \approx 9C^o$. Due to more uniform magnetic field distribution, simple structure has a lower T_{smax} value, but also has a large part of the surface with such increased temperature, see Fig. 2.7d. Due to such a temperature distribution - local higher T_s hot spot in CDS and distributed, but higher T_s value in a simple structure, the quality factor degradation at the RF pulse is

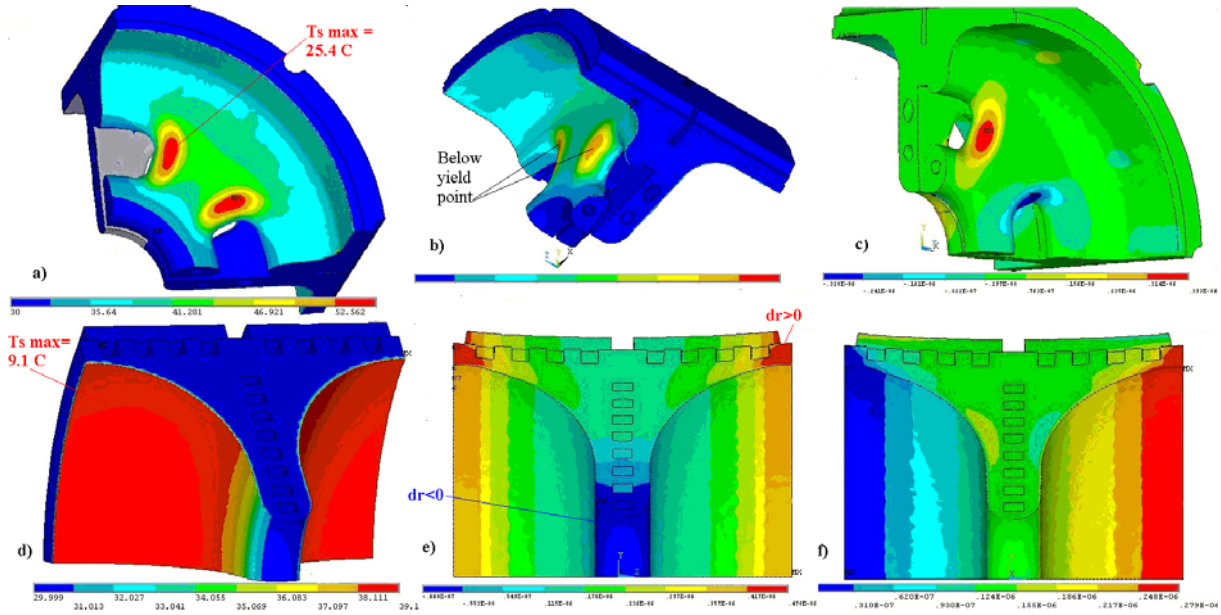

Figure 13: a) - the temperature rise T_s distribution at the CDS ILC cells surface after $\tau = 1000\mu s$ RF pulse, $E_0T = 15\frac{MV}{m}$, b) von Miss stress distribution, c) angular displacements distribution, d) - the temperature rise T_s distribution at the π-mode cell surface for the same τ and E_0T values, e) - radial deformations component, f) - longitudinal displacements in simple structure.

practically the same for both structures and is $\leq 1\%$ in value.

The simple structure has a typical distribution of deformations. The radial component of displacements is shown in Fig. 13e, the longitudinal one - in Fig. 13f. One can see from Fig. 13e, the iris nose displacement inside the cavity (in the region of a strong electric field) and radial displacements outside the cavity at the period ends (in the region of a strong magnetic field). The frequency shift for the simple structure is **negative** and our simulations, with iterative procedure for equilibrium conditions definition [5], show $\delta f \approx -4kHz$.

7 The effect on the cavities RF parameters.

The pulsed cavity RF heating, leading to the surface temperature rise T_s and cavity deformation, results in cavity parameters change during RF pulse, such as own quality factor Q_0 and own cavity frequency change δf during RF pulse.

7.1 Quality factor decreasing and field degradation

The cavity surface heating with the temperature rise T_s, during RF pulse, leads to the natural σ_c decreasing. Decreasing of copper electric conductivity σ, leads to surface resistance R_s, (1) increasing and, assuming a constant magnetic field value at the surface, RF loss power rise. The own cavity quality factor Q_0 is:

$$Q_0 = \frac{2\pi f W_f}{P_{rf}} = \frac{2\pi f \mu_0 \int_v |H|^2 dV}{R_s \int_s |H_\tau|^2 dS}, \quad W_f = \frac{\mu_0}{2}\int_v |H|^2 dV, \quad P_{rf} = \frac{R_s}{2}\int_s |H_\tau|^2 dS, \qquad (12)$$

where W_f is the stored field energy in the cavity and P_{rf} is the total RF losses. With the constant RF power P_i from the klystron, all RF power, supplied in the cavity, should be dissipated in heat at the cavity surface. Let us neglect RF power reflection from the cavity or consider reflected RF power P_{ref} as small $P_{ref} \ll P_i$. If we suppose the constant RF power dissipation in the cavity, but surface resistance increases during RF pulse, **it can be realized only by appropriate reduction in H_τ value at the surface and the corresponding E, H reduction in the cavity volume**. It leads to the W_f reduction and Q_0 decreasing, according (12).
We assume that for the copper electric conductivity σ the usual linear dependence on material temperature is:

$$\sigma = \frac{\sigma_{ref}}{1 + \alpha_T(T - T_{ref})}, \tag{13}$$

where σ_{ref} is the copper electric conductivity value at reference temperature T_{ref} (in handbooks σ_{ref} value is usually given for $T_{ref} = 20C^o$), $\alpha_T \approx \frac{1}{273}$ is the linear coefficient. Let us suppose the T_{ref} value as the equivalent (or averaged) cavity surface temperature before RF pulse. In this case in (13) $T - T_{ref} = T_s$. Supposing $P_{rf} = const$, and taking into account (1), from (12) one can get:

$$R_s \sim \sqrt{1 + \alpha T_s}, \quad E \sim H \sim \sqrt{\frac{P_i}{\sqrt{1 + \alpha T_s}}}, \quad Q_o \sim \frac{Q_{0ref}}{\sqrt{1 + \alpha T_s}}. \tag{14}$$

The dependences of E and Q_0 reductions on time during RF pulse are clear from the expressions in (14) and $T_s \sim \sqrt{t}$ dependence (4). To find values, we have to take into account T_s and P_d distributions at the cavity surface. The calculated value for RF losses increasing for RF Gun cavities for $\tau = 1000\mu s$, $P_i = 8MW$ and T_s distributions at the cavities surface, shown in Fig. 1.7, is $\approx 8.4\%$. It should result in the same relative Q- factor reduction and $\approx 4.2\%$ field reduction at the RF pulse end. For other P_i and τ values it can be estimated by using scaling relations for T_s and dependences in (14).

7.2 Frequency shift estimation

The RG Gun frequency shift δf during RF pulse was estimated in experiments [9] by a special method with the RF signal decay treatment. Let us remind that our simulations show another sign for δf.
We can consider another method for δf estimation, based on the treatment of experimental data for forward and reflected waves parameters. In Fig. 14 the experimental data for forward and reflected power (Fig. 14a) during RF pulse, vector sum and phase (Fig. 14b, Fig. 14c) of the resulting wave in the waveguide are plotted for Gun 3 operation with $\tau = 900\mu s$, $P_i = 3.51MW$ RF pulse at the PITZ facility. The cavity reflection coefficient is:

$$\rho = \frac{\rho_0 - iQ_l\frac{2\delta f}{f}}{1 + iQ_l\frac{2\delta f}{f}}, \quad \rho_0 = \frac{Q_0 - Q_e}{Q_0 + Q_e}, \quad Q_l = \frac{Q_0 Q_e}{Q_0 + Q_e}, \tag{15}$$

where δf is the cavity detuning with respect to driving signal frequency, ρ_0 is the initial reflection coefficient at resonant frequency due to natural small cavity mismatch, Q_l and Q_e are the loaded and external quality factors of the cavity, respectively.
To use data for vector sum and phase, we have several unknowns - ρ_0 and Q_l values. Instead of phase data (Fig. 14c), which are most precise, for δf approximate estimation we will use

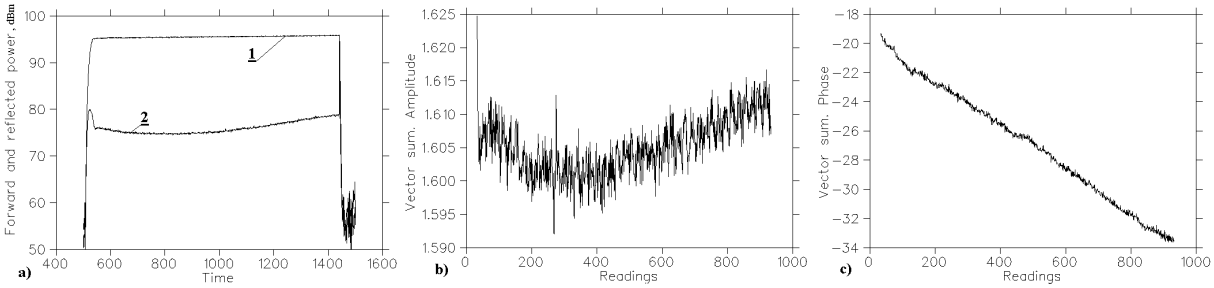

Figure 14: Experimental readings during RF pulse for Gun 3 operation with $\tau = 900\mu s$, $P_i = 3.51MW$ at the PITZ facility. a) - forward (1) and reflected (2) RF power, in dBm, b) vector sum amplitude, c) vector sum phase.

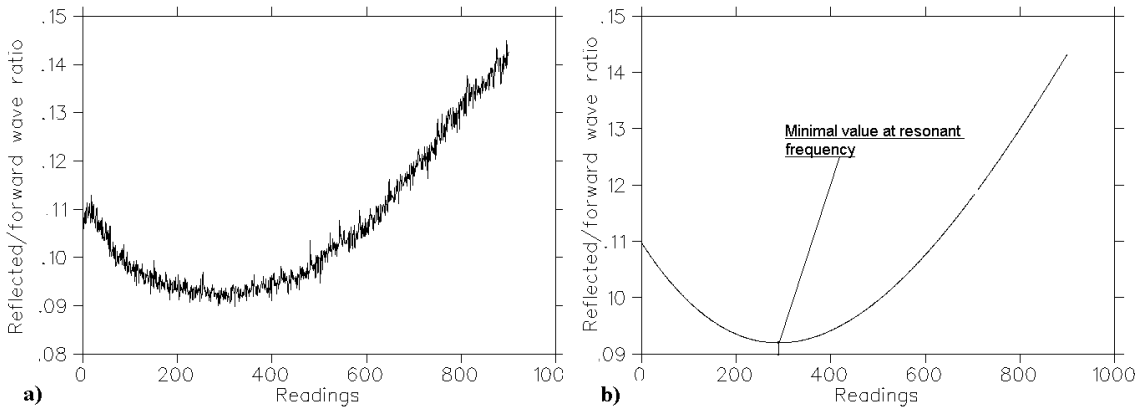

Figure 15: The absolute ρ values, extracted from RF power readings, in original form (a) and after smoothing with third order curve by least-square method (b).

data for forward and reflected RF power. Transferring data, plotted in Fig. 14a from dBm units to Watts, we can find absolute ρ value according to definition as an amplitudes ratio of reflected and forward waves. the obtained data for absolute ρ value are plotted in Fig. 15a in original form and in Fig. 15b after smoothing with third order curve by least-square method.

If we take into account such suggestions, as described in the previous section - Q_0 dependence on the time during RF pulse, hence Q_l and ρ_0 are time dependent, we will get not treatable expression in (15). Moreover, formula (15) is valid for cavities with constant parameters. For δf estimation we will neglect effects, described in the previous Section, considering ρ_0 and Q_l as constant values.

From the plot in Fig. 15b one can find minimal $|\rho| = |\rho_0|$ value at resonant frequency and $|\rho_0| = 0.091957$. Denoting the generalized cavity detuning as $\gamma = \frac{2\delta f}{Q_l f}$, we transform equation (15) to the form:

$$\rho = \frac{(\rho_0 - \gamma^2) - i\gamma(1+\rho_0)}{1+\gamma^2}, \quad |\rho| = \frac{\sqrt{(\rho_0 - \gamma^2)^2 + \gamma^2(1+\rho_0)^2}}{1+\gamma^2}, \tag{16}$$

By fitting γ value, we can find γ_1, γ_2 values, corresponding to the left and right ends of the curve in Fig. 15b - the RF pulse beginning and end. In this case we have to consider two

options - positive (cavity over matching) and negative (cavity under matching) ρ_0 values. Fortunately, for the given $|\rho_0| = 0.091957$ it is not so important - in (16) ρ_0 is several orders of magnitude greater than γ^2. The generalized cavity detuning at the RF pulse beginning and end are found as $\gamma_1 = 0.0601385, \gamma_2 = 0.1110462$. To define the cavity detuning, one has to know Q_l value. The calculated Q_0-factor for RF Gun cavities is ≈ 23400. Assuming 15% Q_0 reduction due to all possible reasons - surface quality, high operating temperature and also keeping in mind cavity mismatch, we can estimate $Q_l = \frac{0.85Q_0}{2} \approx 10000$. For operating frequency $f = 1300MHz$, from the given γ_1, γ_2 values we get cavity detuning during the RF pulse $\delta f = -11.1kHz$.
For the RF pulse parameters $\tau = 900\mu s$, $P_i = 3.51MW$, using $S_f \approx -3.0\frac{kHz}{ms \cdot MW}$ value, calculated for RF Gun 3 design, we obtain $\delta f_c \approx -9.47kHz$, which is 15% lower than the estimated $\delta f = -11.1kHz$. This disagreement is inside the declared precision for our simulations of a thin not uniformly heated layer and further displacements simulations at the $\approx 10\mu m$ level.

8 Conclusion

As compared to UHF X-band or HF S-band RF devices, in L-band NC cavities the pulsed surface heating has softer behavior, due to lower magnetic field values and lower surface resistance, resulting in much lower RF loss power density. Even for cavities with significant $P_d \sim 4.7 \cdot 10^7 \frac{W}{m^2}$ values in L-band case the surface temperature rise $\sim 50C^o$ takes place mainly due to longer RF pulse $\sim 1ms$.
For the RF pulse time $(1 \div 3)ms$ the heat penetrates into the cavity body at a depth of $(330 \div 440)\mu m$ and the heat propagation can be described well in a 1D thin film approximation. The distribution of the pulsed temperature rise at the cavity surface reflects well the RF loss density distribution. Enough high heat energy $\sim (6 \div 7)kJ$ is stored in a thin heated film during a long RF pulse. A cavity engineering design is not important for pulsed surface temperature rise and for the given cavity shape and operational regime there are no methods for the pulsed surface temperature rise control.
Added to a steady-state surface temperature, the pulsed rise can provide high surface temperature values, at $\sim (60 \div 100)C^o$ higher (depending on engineering design) with respect to cooling water input temperature.
The expansion of a thin pulsed heated film at the cavity surface leads to the cavity deformations. These deformations depend on both RF pulse heating parameters and cavity engineering design. Depending on the cavity design, there can be regions with large deformations concentrations, providing higher possibility for material cyclic fatigue.
Instead of nonlinear surface temperature T_s rise and complicated temperature distribution in the heated surface layer, the cavity deformations and related frequency shift, are proportional to the deposited heat energy. For the constant RF input power value it means a linear rise of the cavity frequency shift during RF pulse. For RF Gun cavities operation with $\tau = 1000\mu s$, $P_i = 8MW$, the calculated frequency shift is $\approx -30kHz$, which is comparable with the cavity bandwidth. Leading to the surface temperature rise, RF pulsed heating leads also to the surface resistance and cavity quality factor reduction. Assuming a constant RF power value from RF source, it should also lead to the field amplitude reduction during RF pulse.
The estimated RF Gun cavity detuning, from forward and reflected power values, is in good

agreement with a numerically calculated value.
Results, presented in this report, are new for study of existing L-band cavities and represents some input for more deep understanding of RF Guns operation with extra high input RF power.
The study of the pulsed RF heating effects should be incorporated in the technology of RF Guns development for operating regimes with $E_c \approx 60\frac{MV}{m}$.

9 Acknowlegments

The authors thank N. Brusova for solid models preparations, Dr. K. Floettmann and Dr. F. Stephan for support of this work, DESY PITZ group for providing experimental data and a lot of peoples, both in INR and in DESY, for valuable discussions, comments and proposals.

References

[1] B. Dwersteg, K. Floettmann, J. Sekutowicz, Ch. Stolzenburg. RF gun design for TESLA VUV Free Electron Laser, NIM A 393, p.93-95, 1997

[2] V.V. Paramonov, N.I. Brusova, F. Stephan et al., Design parameters of the normal conducting booster cavity for the PITZ-2 test stand. Proc. 2004 Linac Conference, Lubec, p. 204, 2006

[3] D. Pritzkau. RF Pulsed Heating. Ph.D. Thesis, SLAC-R-577, 2001.

[4] Perry B. Wilson. Scaling linear colliders to 5 TeV and above. In ITP Conf. on Future High Energy Colliders. Univ. of California, Santa Barbara, Oct. 1996.

[5] S.C. Joshi, V.V Paramonov, A.K. Skasyrskaya. The complete 3D coupled RF-thermal-structural-RF analysis ... LINAC02, p. 216, 2002.

[6] K. Floettmann, private communication.

[7] F. Marhauser. High power test of a high duty cycle RF photoinjector gun for the BESSY FEL. EPAC2006, p.68, 2006.

[8] L.D. Landau, E.M. Lifshiz. Theoretical physics. Theory of Elasticity. Moscow, Nauka, 1988.

[9] D. Kotthaus. Design of the Control for the RF Gun of the VUV-FEL Linac. Diplomarbeit. Univ. of Hamburg, 2004.

[10] V.V. Balandin et. al., The positron injector linac for TESLA, Proc. EPAC 2000, p. 462, 2000.

[11] V.V. Paramonov, et al., The PITZ booster cavity - a prototype for the ILC positron injector cavities. PAC 2005, p. 1030, 2005.

[12] J.W. Wang, et al., Studies of Room Temperature Structures for the ILC Positron Source. PAC 2005, p. 2827, 2005.